# Mitochondrial oxidant stress in locus coeruleus is regulated by activity and nitric oxide synthase

**J. Sanchez–Padilla**[1], **J.N. Guzman**[1], **E. Ilijic**[1], **J. Kondapalli**[1], **D.J. Galtieri**[1], **B. Yang**[1], **S. Schieber**[3], **W. Oertel**[3], **D. Wokosin**[1], **P. T. Schumacker**[2], and **D. J. Surmeier**[1]

[1]Department of Physiology, Feinberg School of Medicine, Northwestern University, Chicago, IL 60611 USA

[2]Department of Pediatrics, Feinberg School of Medicine, Northwestern University, Chicago, IL 60611 USA

[3]Department of Neurology, Philipps University, Marburg, Germany

## Summary

Loss of noradrenergic locus coeruleus (LC) neurons is a prominent feature of aging–related neurodegenerative diseases, like Parkinson's disease (PD). The basis of this vulnerability is not understood. To explore possible physiological determinants, LC neurons were studied using electrophysiological and optical approaches in *ex vivo* mouse brain slices. These studies revealed that autonomous activity in LC neurons was accompanied by oscillations in dendritic $Ca^{2+}$ concentration attributable to opening of L–type $Ca^{2+}$ channels. This oscillation elevated mitochondrial oxidant stress and was attenuated by inhibition of nitric oxide synthase. The relationship between activity and stress was malleable, as arousal and carbon dioxide, each increased the spike rate, but differentially affected mitochondrial oxidant stress. Oxidant stress also was increased in an animal model of PD. Thus, our results point to activity–dependent $Ca^{2+}$ entry and a resulting mitochondrial oxidant stress as factors contributing to the vulnerability of LC neurons.

Noradrenergic (NA) LC neurons innervate much of the brain, serving to maintain wakefulness as well as to modulate neural activity and plasticity during periods of arousal and stress [1,2]. Despite their importance, this small group of brainstem neurons is vulnerable to aging and aging–related neurodegenerative diseases, like PD and Alzheimer's disease. The loss of LC neurons might contribute to many of the non–motor symptoms that

Correspondence: D. James Surmeier, Ph.D., Department of Physiology, Feinberg School of Medicine, Northwestern University, 303 E. Chicago Ave., Chicago, IL 60611 USA, (j–surmeier@northwestern.edu).

accompany these diseases, including memory deficits, depression, and daytime hypersomnolence [3].

Why LC neurons are at risk is not clear. One theory of the aging–related decline in neural function is that it reflects a bioenergetic insufficiency stemming from mitochondrial dysfunction [4,5]. Neurons require mitochondrial oxidative phosphorylation to meet their bioenergetic needs. In regions like the substantia nigra pars compacta (SNc), where there is a clear aging–related decline of neuronal number and function, mitochondrial DNA deletions of the type produced by oxidant stress are significantly higher than in unaffected brain regions[6]. Thus, declining mitochondrial function is likely to be a consequence of cumulative oxidant stress [5]. Recessive genetic mutations that increase the risk of PD boost this oxidant stress and create deficits in mitochondrial quality control that could amplify the long–term consequences of oxidant damage[7].

Mitochondrial oxidant stress can arise from either extrinsic or intrinsic sources. Extrinsic oxidant stress can arise when non–mitochondrial processes, such as lysosomal degradation of proteins, generate reactive oxygen species (ROS) that enter mitochondria [8,9]. Intrinsic oxidant stress can arise when ROS are generated by electron leakage from the electron transport chain (ETC) [7]. This oxidant stress can be amplified by genetic or pharmacological perturbations that alter the balance between ROS generation and clearance. In SNc dopaminergic neurons, whose loss is responsible for the cardinal motor symptoms of PD[10], intrinsic mitochondrial oxidant stress has been traced to $Ca^{2+}$ entry through L–type channels during autonomous pacemaking [11]. $Ca^{2+}$ entering through these channels is weakly buffered by cytosolic proteins, allowing it to be taken up by the endoplasmic reticulum (ER) and then passed to mitochondria [12]. Mitochondrial $Ca^{2+}$ entry de–represses enzymes of the tricarboxylic acid cycle, increasing the production of reducing equivalents for the electron transport chain and respiration[13]. However, the precise mechanism by which mitochondrial $Ca^{2+}$ augments oxidant generation is not fully established.

The studies reported here draw strong parallels between the physiological determinants of vulnerability in SNc and LC neurons, showing that activity–dependent opening of L–type $Ca^{2+}$ channels leads to mitochondrial oxidant stress. As in SNc dopaminergic neurons, this stress is exacerbated by deletion of *DJ–1,*a gene linked to an early onset form of PD, and alleviated by antagonism of L–type $Ca^{2+}$ channels. Our work on LC neurons makes four additional points of importance. First, L–type channels with a Cav1.3 pore–forming subunit make a significant contribution to $Ca^{2+}$ oscillations. Second, the endoplasmic reticulum plays an important role in the genesis of mitochondrial oxidant stress. Third, the relationship between activity and oxidant stress is not fixed, but subject to modulation. Fourth, activity–dependent oxidant stress depends on a mitochondrial form of nitric oxide synthase (NOS).

## Results

### L–type channels are engaged during neuronal spiking in LC

Initially, the LC region was mapped using immunocytochemical techniques in *ex vivo* brain slices so that NA neurons were reliably sampled (Fig. 1a, Supplementary Figure 1). In addition, neurons were filled with biocytin and subsequently reconstructed to verify their

identity (Fig. 1a). As previously reported [14], LC NA neurons in *ex vivo* brain slices at physiological temperatures are spontaneously active, spiking at 1–6 spikes/sec (Fig. 1b). Their spiking rate did not change with the addition of glutamatergic and GABAergic synaptic blockers, suggesting that LC neurons were autonomous pacemakers [14]. Another signature feature of LC neurons described previously [15-18] was the presence of small spikelets (20–30 mV amplitude) following blockade of Nav1 channels with tetrodoxin (TTX) (Fig. 1b). The spikes of LC neurons were broad, being 2.5 msec in duration at half–amplitude (Fig. 1c).

Previous studies using somatic recording have implicated engagement of Cav1 L–type channels during autonomous spiking in LC neurons [14,16,17]. To pursue this suggestion, LC neurons were loaded with a low concentration of $Ca^{2+}$–sensitive dye (Fluo–4, 50 μM) and two photon laser scanning microscopy (2PLSM) was used to monitor changes in intracellular $Ca^{2+}$ concentration at dendritic locations. Autonomous spiking was accompanied by phase–locked fluctuations in dendritic $Ca^{2+}$ concentration (Fig. 2a). Moreover, consistent with previous studies, these dendritic $Ca^{2+}$ oscillations were still present following blockade of Nav1 channels with TTX and were eliminated by bath application of the Cav1 channel antagonist isradipine (1 μM) (Fig. 2a)[15,16].

To determine the molecular identity of the channels expressed by LC neurons, they were subjected to quantitative PCR (qPCR) analysis. LC neurons expressed mRNA for both the Cav1.3 pore–forming subunit of the L–type channel and the Cav1.2 subunit (Fig. 2b). Functional expression of Cav1channels was verified by somatic voltage clamp measurements (Supplementary Figure 2). Application of the Cav1.3 selective antagonist BPN4689 (50 μM) [19] significantly attenuated $Ca^{2+}$ spikes and intracellular $Ca^{2+}$ oscillations in the presence of TTX and the residual oscillatory activity was eliminated by the non–selective L–type channel antagonist isradipine (Fig. 2c).

Although antagonism of Cav1 channels eliminated the dendritic fluctuations in $Ca^{2+}$ concentration, it did not alter pacemaking rate or regularity (Fig. 3a), arguing that, as in SNc DA neurons, Cav1 channels contribute to pacemaking but are not essential for its generation [20]. In agreement with this inference, in the presence of TTX (1 μM), autonomous spiking continued, but at a slower rate (Fig. 3b) – suggesting that proximally generated $Na^+$ spikes were pacing dendritic $Ca^{2+}$ spikes. To test this proposition, ectopic spikes were initiated in the somatic region by injection of brief current pulses through the patch electrode while monitoring dendritic $Ca^{2+}$ fluctuations. These ectopic somatic spikes reset the dendritic $Ca^{2+}$ oscillations, as predicted (Supplementary Figure 3).

Quantitative PCR analysis of LC neurons was used to identify channels that help support pacemaking in addition to Cav1 channels. This revealed robust expression of mRNA for voltage–dependent $Na^+$ channels (Nav1.1, 1.2,1.6) and $Na^+$ 'leak' channels (NALCN). Both types of Na+ channels are inward conducting, causing depolarization at sub–threshold membrane potentials. The expression of mRNA for NALCN was significantly greater in LC neurons than in SNc DA neurons, suggesting a more central role in pacemaking. To verify functional expression of NALCN channels, extracellular $Na^+$ was replaced with channel impermeable N–methyl–D–glucamine in the presence of TTX and isradipine (to eliminate

the contribution of Nav1 and Cav1 channels respectively); this intervention hyperpolarized LC neurons by ~20 mV, supporting the proposition that NALCN channels make an important contribution to the membrane potential near spike threshold (Supplementary Figure 4).

Although L–type channels were not required for pacemaking, they might enhance the ability of the cell to sustain spiking when driven by extrinsic inputs [20]. This robustness could be manifested by the ability to sustain an elevated spike rate, as this elevation would increase slow inactivation of Nav1 $Na^+$ channels that normally drive pacemaking. To test this idea, spike rate was increased by elevating the extracellular $[K^+]$ while monitoring spike rate for long periods in the non–invasive perforated–patch configuration. In untreated LC neurons, increasing the extracellular $[K^+]$ to 17 mM (from 2.5 mM) led to a sustained elevation in spike rate (Fig. 3c). Antagonizing L–type $Ca^{2+}$ channels had no effect on basal spiking rate either before or immediately after elevating extracellular $K^+$ concentration; however, after approximately 20 minutes, spike rate fell in the presence of isradipine (Fig. 3c), suggesting that L–type channels help to maintain spiking in this condition.

## Spiking triggers $Ca^{2+}$–induced mitochondrial oxidant stress

In SNc DA neurons, $Ca^{2+}$ is less efficiently buffered by cytosolic proteins than in neighboring VTA DA neurons, allowing it to diffuse in the cytoplasm more readily [21]. In LC neurons, the situation was similar. Intrinsic $Ca^{2+}$ buffering was estimated using the added extrinsic buffer method [22]. The amplitude and decay time constant of the fluorescence signal evoked by a spike was monitored continuously after rupturing the membrane at the tip of a cell–attached patch electrode filled with Fluo–4 (200 μM). As the dye filled the cell, the relative amplitude of the fluorescence signal fell and the time constant rose (Fig 4a, Supplementary Figure 5). These parameters allowed the intrinsic buffering ($K_B$) to be estimated (Fig. 4a). The median $K_B$ for LC neurons was just greater than 50 (the smaller the number the lower the intrinsic buffering). This $K_B$ estimate was similar to that for SNc DA neurons and significantly lower than for neurons with strong $Ca^{2+}$ buffering (e.g., cerebellar Purkinje neurons $K_B$=2000, [23]).

Given the relatively low intrinsic buffering capacity of LC neurons, $Ca^{2+}$ entering the cytoplasm could reach the ER, potentially evoking $Ca^{2+}$–induced $Ca^{2+}$ release (CICR)[12]. To test this possibility, RYRs were antagonized by application of ryanodine (10 μM). Doing so decreased the dendritic $Ca^{2+}$ transients evoked by pacemaking, demonstrating that RYR–dependent CICR was contributing to the observed $Ca^{2+}$ oscillation (Fig. 4b).

In SNc DA neurons, $Ca^{2+}$ entry through plasma membrane L–type channels leads to increased mitochondrial oxidant stress. To determine if the situation was the same in LC neurons, *ex vivo* slices were prepared from transgenic mice expressing a mitochondrially targeted ratiometric redox probe mito–roGFP [11,24] under control of the cytomegalovirus (CMV) promoter (Fig.5a). LC neurons exhibited a basal mitochondrial oxidant stress that was typically 40–50% of the dynamic range of the probe (Fig. 5a). Antagonizing plasma membrane L–type channels with isradipine dose–dependently diminished this stress without altering pacemaking (Fig. 5b–c). Blocking $Ca^{2+}$ entry into mitochondria with the

mitochondrial uniporter (MCU) blocker RU360 (10 μM), also virtually eliminated oxidant stress (Fig. 5b–c) without changing pacemaking rate (data not shown).

Mitochondrial $Ca^{2+}$ entry is widely thought to occur at junctions between the ER and mitochondrion where the local $Ca^{2+}$ concentration can rise into the micromolar range [25]. Both RYRs and inositol trisphosphate receptors (IP$_3$Rs) populate these junctions (referred to as mitochondria–associated membrane or MAMs)[26]. Consistent with the idea that mitochondrial $Ca^{2+}$ entry was occurring at MAMs, antagonizing RYRs profoundly lowered mitochondrial oxidant stress, diminishing it by roughly the same amount as blocking the MCU with RU360 (Fig. 5b–c). These results suggest that plasma membrane $Ca^{2+}$ entry through L–type channels is sequestered by the ER and then passed through RYRs to mitochondria, leading to oxidant stress (Fig. 5b–c).

Mitochondrial oxidant stress was accompanied by fluctuations in the mitochondrial membrane potential as measured with the cationic dye tetramethyl rhodamine methylester (TMRM). These potential fluctuations had a frequency in the range of 10–30 milliHz and amplitudes of about 10% of the TMRM dynamic range (Fig. 5d), suggesting that they were attributable to opening and closing of an ion channel in the inner mitochondrial membrane. The frequency and amplitude of fluctuations were diminished by genipin (100 μM), an inhibitor of uncoupling proteins (UCPs) – ion channels that are capable of depolarizing the inner mitochondrial membrane [27] (Fig. 5e). The potential fluctuations also were attenuated in frequency and amplitude by diminishing $Ca^{2+}$ entry through plasma membrane L–type channels (Fig. 5f).

### Oxidant stress is elevated in LC neurons lacking DJ-1

Loss of function of DJ–1 protein is associated with autosomal recessive early onset forms of PD in humans[7], and has been described as a redox–sensitive protein that participates in orchestrating oxidant defense [28]. Previous studies have shown that deletion of DJ–1 exacerbated mitochondrial oxidant stress in SNc and DMV neurons[11,29]. If mitochondrial oxidant stress is a driver of LC degeneration, it should be increased in mice lacking functional DJ–1. To test this hypothesis, stereotaxic injection of an AAV viral vector was used to deliver a CMV–mito–roGFP expression construct to LC neurons in *DJ–1* knockout (*DJ–1$^{-/-}$*) and wild–type mice. Ten to fourteen days later, brain slices were prepared and oxidant stress assayed as described above. These experiments were done at room temperature, since previous studies showed that probe oxidation was nearly complete at physiological temperatures[11]. In LC neurons from *DJ–1$^{-/-}$,* mitochondrial oxidant stress was significantly greater than in wild–type mice (Fig. 5g). Moreover, antagonism of L–type channels significantly attenuated mitochondrial oxidant stress in *DJ–1$^{-/-}$* neurons (Fig. 5g).

### Extrinsic signals differentially regulate oxidant stress

The activity of LC neurons varies with behavioral state [1], raising the possibility that oxidant stress varies in parallel. For example, during sleep the activity of LC NA neurons is suppressed by GABAergic input [30], which could lessen mitochondrial stress. Indeed, application of the GABA$_A$ receptor agonist muscimol hyperpolarized LC neurons, stopped spiking and dramatically diminished mitochondrial oxidant stress (Fig. 6a–b). Conversely,

during arousal the discharge rate of LC NA neurons increases, which could augment mitochondrial oxidant stress. The increase in LC discharge rate during arousal is attributed to the release of orexin in the LC by hypothalamic neurons [31-33]. Bath application of orexin increased the discharge rate of LC neurons in our preparation (as predicted) (Fig. 6a). Yet surprisingly, orexin attenuated, rather than increased, mitochondrial oxidant stress (Fig. 6b). One possible explanation of this change is that orexin altered the pacemaking mechanism to rely more upon $Na^+$ channels and less upon the opening of L–type $Ca^{2+}$ channels[34]. To test this hypothesis, two experiments were performed. First, if orexin inhibited L–type channels, then spiking in the presence of TTX (which depends upon L–type channels) should be impaired. Indeed, orexin virtually eliminated spiking in the presence of TTX (Fig. 6c). Second, inhibition of L–type channels should decrease dendritic $Ca^{2+}$ transients during normal pacemaking. As predicted, orexin significantly diminished these transients (Fig. 6d). Thus, mitochondrial oxidant stress in LC neurons is state dependent, falling both during GABAergic suppression of activity and during orexin–mediated acceleration of activity.

Hypercapnia also increases the spiking rate of LC neurons [15,16], which may contribute to the modulation of breathing. Moreover, hypercapnia–induced acceleration in the spiking of LC neurons is dependent upon L–type $Ca^{2+}$ channels [15,16], suggesting hypercapnia might increase mitochondrial oxidant stress. To test this hypothesis, LC neurons in brain slices were bathed in a solution bubbled with gas containing 15% carbon dioxide ($CO_2$) to induce hypercapnia. As shown previously, hypercapnia increased the spiking rate of LC neurons monitored in cell–attached recording mode (Fig. 6e). To determine if mitochondrial oxidant stress was affected, slices were bathed in the hypercapnic solution for 1 hour and then mitochondrial redox status was assessed using 2PLSM. As predicted, hypercapnia significantly increased mitochondrial oxidant stress relative to slices maintained in the normal 5% $CO_2$ environment (Fig. 6f).

## Oxidant stress was dependent upon nitric oxide synthase

How does $Ca^{2+}$ entry into mitochondria elevate oxidant stress? There is no consensus on this point. Mitochondrial $Ca^{2+}$ influx de–represses matrix dehydrogenases of the tricarboxylic acid (TCA) cycle, leading to increased generation of electron donors for the ETC[13]. In physiological circumstances, increasing the proximal flux of electrons into the ETC could increase the production of superoxide and other reactive oxygen species (ROS) [35]. However, there are other ways in which mitochondrial $Ca^{2+}$ entry might increase ROS production. For example, sustained $Ca^{2+}$ influx into mitochondria could stimulate a mitochondrial form of NOS [36,37]. NO produced by NOS activation competes with $O_2$ at cytochrome oxidase, thereby changing the redox status at earlier points along the ETC and increasing the production of superoxide [37]. To determine if these mechanisms were at work in LC neurons, cells were loaded with the NO–sensitive probe 4–amino–5–methylamino– 2,7–difluorescein (DAF–FM) with a local perfusion pipette;then neurons were imaged using 2PLSM. In unperturbed LC neurons, DAF–FM fluorescence was readily detectable (Fig. 7a, Supplementary Figure 6). The NO signal was decreased by pre–incubation with the NOS inhibitor L–$N^G$–nitroarginine methyl ester (L–NAME, 100 μM) (Fig. 7a). Antagonizing plasma membrane L–type channels also decreased the DAF–FM signal (Fig. 7b). Although the source of NO could not be determined directly because the dye was largely cytosolic,

blocking $Ca^{2+}$ entry into mitochondria with RU–360 decreased the cytosolic NO signal (Fig. 7b), arguing that mitochondria are a site of origin. Conversely, blocking $Ca^{2+}$ efflux from the mitochondria by antagonizing the mitochondrial $Na^+$–$Ca^{2+}$ exchange (NCX) with 5 μM CGP37157[26,38], led to an increased cytosolic NO signal (Fig. 7b), arguing that increasing intramitochondrial $[Ca^{2+}]$ stimulates NO production.

To determine if NO production increased mitochondrial oxidant stress, slices were incubated with L–NAME (100 μM) prior to determining the redox status of mitochondria. Previous work has shown that NO does not directly alter mito–roGFP fluorescence, so any change in these experiments is attributable to altered dithiol formation [39]. Pre–incubation with L–NAME significantly diminished mitochondrial oxidant stress in LC neurons (Fig. 7c). L–$N^G$–nitroarginine (L–NNA, 10 μM), a different NOS inhibitor also decreased mitochondrial oxidant stress (Fig. 7c). Exposure of SNc DA neurons to L–NAME had a very similar effect (Fig. 7c), suggesting that NOS activity was a significant source of oxidant stress in both cell types. To provide an additional test of the inference that NOS activity was increasing mitochondrial oxidant stress, TMRM was used to monitor mitochondrial membrane potential. As predicted, L–NAME significantly diminished the amplitude and frequency of fluctuations in mitochondrial potential (Fig. 7d).

## Discussion

Three conclusions can be drawn from the studies presented. First, LC NA neurons have a robust pacemaking phenotype that leads to basal mitochondrial oxidant stress that is exacerbated in a genetic model of PD. Second, although mitochondrial stress generally tracked spike activity and $Ca^{2+}$ entry through L–type channels, this relationship was subject to modulation. Third, the activity–dependent oxidant stress stems in large part from stimulation of a mitochondrial form of NOS. These conclusions provide a framework for understanding how age and disease might lead to the loss of LC NA neurons, as well as how this loss might be averted.

### Spiking elevates oxidant stress in LC neurons

Previous work on LC neurons has not provided a mechanistic foundation for understanding their sensitivity to aging and aging–related neurodegenerative diseases, like PD and AD. A number of studies have shown that LC neurons are spontaneously active and this activity is autonomously generated [14,15]. Our results were consistent with these studies and extend them in several important respects.

Using 2PLSM $Ca^{2+}$ imaging approaches, it was revealed that autonomous pacemaking was accompanied by large fluctuations in dendritic $Ca^{2+}$ concentration attributable to opening of a mixture of L–type channels with Cav1.3 and Cav1.2 pore–forming subunits. As in SNc DA neurons, the low–threshold Cav1.3 L–type channels in LC neurons were active throughout the interspike interval, leading to a sustained $Ca^{2+}$ influx. Although $Ca^{2+}$ current through L–type channels contributed to the inward currents driving LC pacemaking, they were not necessary to maintain it, as low micromolar DHP concentrations virtually eliminated dendritic fluctuations in intracellular $Ca^{2+}$ concentration, but had no effect on pacemaking rate and regularity.

Although not necessary for pacemaking, L–type channels increased the robustness of pacemaking. In fact, dendritic L–type $Ca^{2+}$ channels sustained pacemaking after blocking Nav1 channels with TTX, albeit at a lower rate. This contrasts with the situation in SNc DA neurons where L–type channels are capable of only sustaining a sub–threshold dendritic oscillation after block of Nav1 channels [40]. For this type of $Ca^{2+}$–dependent dendritic pacemaking to work, $Ca^{2+}$ must be weakly buffered by cytosolic proteins so as to allow free $[Ca^{2+}]$ to control the onset of repolarization by $Ca^{2+}$ activated $K^+$ channels [41]. As a consequence, much of the entering $Ca^{2+}$ must be slowly sequestered by intracellular organelles. The ER is widely viewed as a key mediator of intracellular $Ca^{2+}$ buffering on this time scale [42]. Although ER $Ca^{2+}$ content was not monitored, it was found that blocking ER RYRs diminished cytosolic $Ca^{2+}$ transients during pacemaking, suggesting that the ER was playing an important role in intracellular $Ca^{2+}$ dynamics. In many cell types, ER buffering leads to $Ca^{2+}$ being shuttled to mitochondria at specialized junctions, so–called MAMs [26]. RYRs are localized on the ER side of MAMs and MCUs are found on the mitochondrial side, creating a mechanism by which $Ca^{2+}$ can move from the ER to mitochondria. This same arrangement appears to be present in LC neurons, where $Ca^{2+}$ shuttled into mitochondrial was sufficient to create an oxidant stress as measured with a matrix–targeted redox–sensitive variant of GFP.

Given the negative consequences of sustained $Ca^{2+}$ entry, why do LC NA neurons express such high levels of the Cav1 channel? One possibility is that $Ca^{2+}$ drives the synthetic machinery necessary for proper functioning of LC neurons [43]. Another possibility is that the pacemaking function of LC NA neurons is essential for organismal fitness and survival. During waking states, even a transient loss of spiking in LC NA neurons results in impaired brain function, which could be catastrophic (if, for example, one were being pursued by a predator). This would create evolutionary pressure to put in place redundant pacemaking mechanisms that minimize the likelihood of failure even with sustained excitation. In slices, LC NA neurons were able to continue spiking at elevated rates for as long as the recording could be sustained. However, in the presence of L–type channel antagonists, spiking was less robust, failing within about 20 minutes after increasing extracellular $K^+$. This difference is attributable to the fact that, unlike Cav1 $Ca^{2+}$ channels, Nav1 $Na^+$ channels are subject to slow, voltage–dependent inactivation with sustained depolarization. So, it is easy to imagine that there would be strong evolutionary pressure to creating a 'backup' dendritic oscillator that was not going to fail under the same conditions – an oscillator like that involving Cav1 $Ca^{2+}$ channels. The cost of this design choice is the sustained elevation in mitochondrial oxidant stress. However, this cost is one that could be tolerated, as there are biochemical systems in place to mitigate oxidant stress and delay its negative consequences. Indeed, the impact on the function of the LC NA system takes five or six decades to become manifest, which is well beyond the life expectancy of animals with this design, including humans until recently.

## Mitochondrial stress was state–dependent

The engagement of the dendritic oscillator was modulated by extrinsic inputs. During sleep, the autonomous activity of LC NA neurons is actively suppressed by GABAergic input [30,44]. This suppression could be mimicked in *ex vivo* brain slices by application of the

$GABA_A$ receptor agonist muscimol. As expected, suppression of pacemaking diminished $Ca^{2+}$ entry and mitochondrial oxidant stress. In contrast, arousal leads to an elevation in the spiking rate of LC neurons, increasing the release of NA in brain regions controlling behavioral activation[45]. One of the drivers of this type of arousal is orexin, which is released by hypothalamic neurons innervating the LC[31]. As anticipated, exogenous orexin significantly increased the discharge rate of LC neurons in brain slices. What was not anticipated was that this increase in discharge rate would lead to *lowered* mitochondrial oxidant stress. This happened because orexin negatively modulated L–type channel opening while increasing $Na^+$ currents, presumably those through NALCN channels. This observation is consistent with early work showing that the effects of orexin on LC spiking was independent of $Ca^{2+}$[34]. It is not clear at this point how this modulation was brought about, but L–type $Ca^{2+}$ channels are well known to be regulated by G–protein coupled receptors, like those mediating the effects of orexin.

Hypercapnia also increased the spiking rate of LC neurons. Augmented LC spiking is thought modulate brainstem respiratory circuits, promoting increased respiratory rate [46]. However, unlike the response to orexin, the excitatory effects of hypercapnia depend upon L–type $Ca^{2+}$ channels in LC neurons [15,16]. Accelerating the discharge rate of LC neurons without suppressing the opening of L–type $Ca^{2+}$ channels should lead to increased $Ca^{2+}$ entry and mitochondrial $Ca^{2+}$ loading. Indeed, hypercapnia increased mitochondrial oxidant stress in LC neurons. These results suggest that persistent respiratory insufficiency could have a negative impact on LC and contribute to neurodegenerative decline.

### Mitochondrial $Ca^{2+}$ entry stimulated NOS and oxidant stress

$Ca^{2+}$ that enters the mitochondrial matrix stimulates oxidative phosphorylation by de–repressing dehydrogenases, thereby helping to meet bioenergetic needs [37]. Our results suggest that another consequence of mitochondrial $Ca^{2+}$ entry is stimulation of NOS. NO production, as measured with cytosolic DAF–FM, was robust in pacemaking LC neurons. Not only was NO production sensitive to $Ca^{2+}$ entry through plasma membrane L–type channels, it was sensitive to antagonism of the mitochondrial uniporter with RU360. Moreover, while blocking entry decreased NO production, disrupting removal of $Ca^{2+}$ from the matrix by NCX *increased* NO levels. The ability of L–NAME to block NO production suggests the involvement of an enzymatic process, again implicating NOS. Studies in other tissues have shown that a $Ca^{2+}$–dependent form of NOS is localized to mitochondria [36], providing a clear precedent for the observations in LC neurons.

What was more unexpected was the observation that inhibition of NOS decreased the oxidation status of matrix proteins and attenuated the fluctuations in mitochondrial potential driven by that stress. This suggests that NOS contributes to oxidant stress. How? NO generated in proximity to the electron transport chain can compete with $O_2$ at the binuclear center of cytochrome oxidase, leading to an increase in the reduction state of more proximal electron carriers and to an increase in the generation of superoxide [37].

But what end does this signaling pathway serve? One possibility is that NO generated in response to mitochondrial matrix $Ca^{2+}$ entry helps to prevent $Ca^{2+}$ overload; that is, it serves as a negative feedback regulator of mitochondrial calcium uptake. By inhibiting cytochrome

oxidase, NO can slow electron transport, leading to a decrease in mitochondrial membrane potential and a slowing of mitochondrial $Ca^{2+}$ influx. By regulating matrix $[Ca^{2+}]$, this mechanism would prevent activation of the mitochondrial permeability transition pore (mPTP), which could inflict lethal injury on the cell [7]. This model is consistent with the demonstration that TCA enzymes are more sensitive to $Ca^{2+}$ than is mitochondrial NOS [13]. Thus, modest mitochondrial $Ca^{2+}$ entry can maintain oxidative phosphorylation necessary for neuronal survival[47], without activating NOS. However, when mitochondrial $Ca^{2+}$ influx increases, NOS–mediated NO production would lead to an inhibition cytochrome oxidase, a slowing the ETC and a diminished driving force for $Ca^{2+}$ entry [37]. This 'braking' mechanism also provides a compelling rationale for the expression of NOS in the mitochondria, as this localization confers sensitivity to matrix $Ca^{2+}$ that would not be detected by NOS expressed in the cytosol. An unfortunate by–product of this mechanism is the production of superoxide by the ETC [7,47]. However, in most neurons, the engagement of the NOS brake (and the production of superoxide) should be infrequent. LC NA neurons (and SNc DA neurons) are exceptions, where large and sustained mitochondrial $Ca^{2+}$ influx leads to the continuous activation of this protective brake. During a typical human lifespan, the cumulative oxidant damage produced by this mechanism could contribute to mitochondrial DNA defects that impair the ability to generate ATP, leading to bioenergetic failure and cell death [5,6].

As appealing as the model is, there is an alternative explanation for our DAF–FM data that needs to be considered. For DAF–FM fluorescence to increase with NO exposure, its amide group must be oxidized[48]. Could the dependence of the DAF–FM signal on mitochondrial $Ca^{2+}$ entry arise from 'enabling' mitochondrial ROS generation and not mitochondrial localization of NOS? This seems highly unlikely as an extra–mitochondrial NOS localization would leave unexplained the ability of NOS–inhibitors to diminish mitochondrial matrix oxidant stress or oscillations in the inner mitochondrial membrane potential.

### Therapeutic strategy in aging–related neurodegeneration

Many of the neurons that succumb to aging and aging–related degenerative diseases have essential physiological functions that require an ability to maintain autonomous spiking under normal and stressful states. In at least three of these cell types – DMV cholinergic neurons, SNc DA neurons and LC NA neurons –the sustained engagement of L–type $Ca^{2+}$ channels enhances the reliability of autonomous spiking, at the cost of increased mitochondrial oxidant stress [11,29]. Our data now confirms that in a mouse model of PD, LC neurons also display exacerbated mitochondrial stress, the latter attenuated in this mouse model by using Cav1 channel antagonists. The engagement of L–type channels during autonomous spiking might be considerably more widespread than previously recognized. Use of Cav1 channel antagonists to lower blood pressure that cross the blood brain barrier have no obvious deleterious neurological consequences for humans and have been linked to reduced risk of developing PD [49] and to slowing of progression. These drugs also might have utility in slowing the progression of AD [50] and the non–motor symptoms of PD, particularly those potentially dependent upon the loss of LC neurons.

## Methods

### Brain slice preparation

Acute pontine horizontal slices (220–μm thick) were prepared from wild–type male C57BL/6 mice (Charles River) or *DJ–1*$^{-/-}$ mice (backcrossed to C57BL/6) between postnatal ages 21 and 32 days, unless specified otherwise. The handling of mice and all procedures performed on them were approved by the institutional Animal Care and Use Committee and were in accordance with the National Institutes of Health Guide to the Care and Use of Laboratory Animals and Society for Neuroscience guidelines. Mice were anesthetized with a ketamine/xylazine mixture, followed by a transcardial perfusion with ice–cold, oxygenated artificial CSF (ACSF) containing the following (in mm): 125 NaCl, 2.5 KCl, 25 NaHCO$_3$, 1.25 NaH$_2$PO$_4$, 2 CaCl$_2$, 1 MgCl$_2$, and 25 dextrose, pH 7.3 (osmolality 315–320 mOsm/L). After perfusion, mice were decapitated and brains removed rapidly, followed by sectioning in ice–cold oxygenated ACSF using a vibratome (VT1000S; Leica Microsystems). Pontine slices were incubated in ACSF at 32–34°C for 30 min before electrophysiological recordings. Slices were then be transferred to a small–volume (<0.5 ml) recording chamber that mounted on a fixed–stage, upright microscope (BX51; Olympus America) equipped with infrared differential interference contrast (0.9 numerical aperture (NA) with de Sénarmont compensation (Olympus). Electrophysiological recordings were performed at 33–34°C, unless specified otherwise. The recording chamber were superfused with carbogen–saturated ACSF with a flow rate of 2–3 ml/min running through an in–line heater (SH–27B with TC–324B controller; Warner Instruments). Neuronal somata and proximal dendrites were visualized by video microscopy at high magnification (60×, 0.9 NA water–immersion objective; Olympus). Brain slices were utilized within 3 hours from slice preparation.

### Electrophysiology

Cell–attached and whole–cell patch–clamp recordings were performed in locus ceruleus (LC) neurons located near the floor of the fourth ventricle. LC neurons were recognized as a cluster of neurons with large somatic compartments. Recording patch electrodes (resistance of 3–6 MΩ) were prepared with a Sutter Instruments horizontal puller using borosilicate glass with filament. For current–clamp recordings, patch electrodes were filled with internal solution containing the following (in mM): 135 K–MeSO$_4$, 5 KCl, 5 HEPES, 0.05 EGTA, 10 phosphocreatine–di(tris), 2 ATP–Mg, and 0.5 GTP–Na, the pH adjusted to 7.3 (osmolality adjusted to 290–300 mOsm/L). The liquid junction potential in our recording ACSF using this internal solution is 7 mV and not corrected for. Conventional tight–seal (>2 GΩ) whole–cell patch–clamp and cell–attached recordings were made on visually identified LC neurons based on (1) size, (2) somatodendritic morphology, and (3) regular spiking between 1 and 6 Hz. Signals were filtered at 1–4 kHz and digitized at 5–20 kHz with a Digidata 1400 (Molecular Devices). For current–clamp recordings, the amplifier bridge circuit were adjusted to compensate for electrode resistance and monitored. For perforated–patch current clamp experiments, internal solution was supplemented with amphotericin–B (Sigma), prepared fresh and added in the internal solution to a final concentration of 180 μg/ml. Alexa568 was added in the internal solution to confirm recordings were done under

perforated–patch mode. Electrode capacitance was compensated and if series resistance increased >20% during recording, the data were discarded.

## 2PLSM Ca$^{2+}$ imaging

For dendritic Ca$^{2+}$ measurements, LC neurons were loaded with internal solutions supplemented with Alexa Fluor 594 (20 μM) and Fluo–4 (50 μM) through the patch pipette. All experiments were performed at 32–34°C. Imaging took place after 15–20 min of dye loading. Images were acquired with an Olympus LUMPFL 60×/1.0 NA water–dipping objective lens. The two–photon excitation source was a Chameleon–ultra1 laser system (690 to 1040 nm) from Coherent Laser Group. Optical signals were acquired using 820 nm excitation (80–MHz pulse repetition frequency and ~250 fs pulse duration) to simultaneously excite Alexa and Fluo–4 dyes. Laser power attenuation was achieved with two Pockels' cell electro–optic modulators (models M350–80–02–BK and M350–50–02–BK; Con Optics) controlled by PrairieView and WinFluor, repsectively. The two cells are aligned in series to provide: enhanced modulation range for fine control of the excitation dose (0.1% steps over five decades), to limit maximum power, and to serve as a rapid shutter during line scan acquisitions. The laser–scanned images were acquired with a Prairie Technologies Ultima system. The fluorescence emission was collected by non–de–scanned photomultiplier tubes (PMTs). The green (490–560 nm) and red (580–630 nm) fluorescence were each detected by a multi–alkali–cathode PMT. The system digitized the current from detected photons to 12 bits. The laser light transmitted through the sample was collected by the condenser lens and sent through a Dodt contrast tube (Luigs and Neumann)to another PMT (R3896, Hamamatsu) to provide a bright–field transmission image (Prairie USB transmission detector) in registration with the fluorescent images. Fluorescence measurements were taken in a sample plane along dendritic segments (80–100 μm from the soma). Line scan signals were acquired at 6 ms per line and 512 pixels per line with 0.18 μm pixels and 10 μs pixel dwell time.

## Endogenous Ca$^{2+}$ buffering capacity

Buffering capacity experiments were adapted to 2PLSM based on protocols described previously by other groups using 200 μM Fluo–4 ($K_d$ = 300 nM, $R_f \approx 85–100$)[22,29]. LC neurons were current clamped and pacemaking was silenced to –60 mV. Somatic fluorescence was imaged as a function of time upon breaking into the cells while inducing spikes to evoke Ca$^{2+}$ transients. Ca$^{2+}$ signal was detected using 2PLSM as described in the previous section (see above). For data analysis, we utilized equations described by Neher and Augustine[51]. In order to measure changes in intracellular Ca$^{2+}$ ( $[Ca^{2+}]$ = $[Ca^{2+}]_{peak}$ – $[Ca^{2+}]_o$), we calculated first $\delta f = (f – f_o)/f_o$ from Ca$^{2+}$ transients evoked by the induced spike (2 ms pulse, 1 nA). $[Ca^{2+}]$ was calculated from equation (1):

$$\frac{\Delta[Ca^{2+}]}{K_d} = \frac{f_{max}}{f_o}(1 - R_f^{-1})\frac{(\delta f)}{[(\delta f_{max} - \delta f)\delta f_{max}]} \quad (1)$$

The value of $\delta f_{max}$ was calculated by a depolarizing current step that achieves a Ca$^{2+}$ plateau to saturate Fluo4 dye. From this value, we calculated resting $[Ca^{2+}]_o$ from equation (2):

$$[Ca^{2+}]_o = \frac{(1 - R_f^{-1})}{\delta f_{max}} - R_f^{-1} \quad (2)$$

The estimated value of $R_f \approx 85\text{--}100$ for Fluo4 was obtained from Maravall et al. [22], making $R_f^{-1}$ value small and therefore, it was disregarded from equations (1) and (2). The dynamic range of the dye ($f_{max}/f_o$) was estimated as $1+\delta f_{max}$. After determining [$Ca^{2+}$] and related parameters, we then calculated added buffering capacity ($K_F$) using equation (3):

$$K_F = \frac{(K_d[Fluo - 4])}{(K_d + [Ca^{2+}]_o)(K_d + [Ca^{2+}]_{peak})} \quad (3)$$

The inverse of [$Ca^{2+}$] was then plotted as a function of added buffering capacity and with a linear regression, the estimated endogenous buffering capacity ($K_B$) was determined from the linear fit intersecting the negative x–axis.

## 2PLSM mito–roGFP imaging

Pontine slices from wild–type, roGFP transgenic mice were incubated in ACSF at physiological temperatures 32–34°C followed by a recovery period at room temperature. Experiments were performed at physiological temperatures with the exception of the experiments using the mouse model of PD. For stereotaxic injections of recombinant adenoassociated virus (rAAV) to drive expression of mito–roGFP under the regulation of the CMV promoter, C57BL6 male mice (>P21 postnatal age) were anaesthetized with isoflurane (induction 2.5%, maintenance 1.5%) delivered continuously with 100% medical $O_2$. Throughout the surgery, mice were placed under a heating pad to avoid hypothermia. Mice were injected subcutaneously with Metacam (0.1mg/ml) and placed in a Kopf stereotaxic frame apparatus with head position to obtain a flat skull between bregma and lambda. A craniotomy was performed using micro–drill to expose brain tissue and recombinant adeno–associated virus (AAV) virus was injected (200 nanoliters) with a glass micropipette (VWR) directly into the LC region using the following stereotaxic coordinates: 5.45 mm posterior to bregma; 1.28 mm lateral to midline; and 3.65 mm deep from the cortical surface. The mitochondrial redox sensitive probe, pFB–AAV–CMV–MTS–roGFP, was generated by cloning EcoR1 –XhoI fragment from TH–SK–MTS–roGFP–pA plasmid into EcoR1–SalI sites of pFB–AAV–CMV– SV40 vector (Virovek). pFB–AAV–CMV– MTS–roGFP–pA DNA was packaged into AAV9–CMV–MTS–roGFP–SV40 by Virovek. The AAVs with 2.4E+13vg/ml titers were injected into LC region to express MTS–roGFP. Following ten to fourteen days post–surgery, brain slices were prepared as described. Optical imaging of roGFP signals acquired using a 920 nm excitation beam in a fixed plane of focus with a pixel size between 0.18–0.21 μm and a 10 μs pixel dwell time. This wavelength was chosen by determining the two–photon excitation spectrum of mito–roGFP in cultured dopaminergic neurons from TH–mito–roGFP mice[11]. Laser was a Chameleon–Ultra1, 690 nm to 1040 nm, 80MHz ~250 fs sample pulse duration, Coherent Laser Group. The roGFP fluorescence was detected (490–560 nm) by a non–de–scanned GaAsP PMT (H7422PA, Hamamatsu) and a laser scanned Dodt contrast transmission PMT (R3896, Hamamatsu) detector system (Prairie Technologies) that provided a bright–field transmission image. Sixty frames of the roGFP signal were collected in one optical plane at

a rate of 3–4 frames per second. Records with drifting baseline (due to photo–bleaching or photo–oxidation of roGFP) were discarded. At the end of all experiments, the maximum and minimum fluorescence of mito–roGFP was determined by application of 2 mM dithiothreitol (DTT) to fully reduce the mitochondria, and then 200 μM aldrithiol (ald) to fully oxidize mitochondria. Relative oxidation was calculated with the equation '1–(($F$–$F_{ald}$)/$F_{DTT}$–$F_{ald}$))'.

**2PLSM imaging of mitochondrial membrane potential**

Brain slices from wild–type were incubated in 2–4 μM TMRM for 30–60 minutes at 32–34°C; excess dye was washed out with a TMRM–free ACSF solution. Imaging experiments were performed with TMRM–free ACSF solution at physiological temperatures (32–34°C). Fluorescence (580–630 nm) was collected by a GaAsP PMT (H7422PA, Hamamatsu) as part of the Prairie Technologies laser scanning microscope. Fluorescence measurements in a region of interest (ROI) were monitored to ensure stationarity of the signal; samples with a drifting baseline (due to photo–bleaching of dye and/or wash–out) were discarded. Time–series scanning (1000 frames) in a fixed plane were performed with a 10 μs dwell time at a rate of 2.5–3 frames per second using the 2PLSM system described above. Four to five ROIs in the cell body and one ROI in the nucleus were monitored and changes in TMRM fluorescence were plotted as a function of time. Flickering frequency is defined as the number of transitions in 100 sec epochs. The change in mitochondrial membrane potential (V) during flickering was estimated from the fluorescence in an ROI using a Nernst equation: $V = (RT/zF)\ln(\beta F_m/F_n)$ where R is the gas constant, T is temperature, F is Faraday's constant, $z=1$, $F_m$ is the fluorescence in the mitochondrial ROI, $F_n$ is the fluorescence of the nucleus in the same optical plane and β is a scaling factor. The scaling factor was calculated by assuming that the mitochondrial membrane potential was –150 mV when $F_{maximal}$. For each flickering event, the percent change in V was calculated by taking the difference in the estimates before and then during the drop in fluorescence; the fluorescence during the drops was averaged.

**2PLSM nitric oxide (NO) imaging**

The NO probe 4–amino–5–methylamino– 2,7–difluorescein (DAF–FM) (Life Technologies) stock was dissolved in DMSO as instructed by the manufacturer. Stock solution was always prepared fresh on the day of the experiment. Following brain slice preparation, DAF–FM was perfused directly into the LC region via a patch pipette filled with 10 μM of the probe, at physiological temperatures (32–34°C) and waited 5–10 minutes prior to 2PLSM imaging. Optical imaging of DAF–FM signals acquired using a 920 nm excitation beam, in a fixed plane of focus with a pixel size between 0.18–0.21 μm and a 10 μs pixel dwell time. DAF–FM fluorescence (490–560 nm) was detected by a GaAsP PMT (H7422PA, Hamamatsu) and a Dodt contrast detector system that provided a bright–field transmission image (Prairie Technologies). For experiments using nitric oxide signaling inhibitor, brain slices were pre–incubated with inhibitors/antagonists for 2 hours, and then perfused with DAF–FM. For pharmacological experiments using isradipine, Ru360, and CGP37157, brain slices were hemi–dissected one sister slice containing LC corresponding to vehicle treatment, and the other sister slice corresponding to respective pharmacological manipulation, using same laser power and PMT settings. DAF–FM fluorescence was normalized by Dodt contrast

signal to control for variations in laser power (as detected in the condenser path), and termed relative DAF–FM fluorescence in the box–plots.

### Quantitative polymerase chain reaction (qPCR)

SNc and LC brain regions were micro–dissected from wild–type and total RNA was extracted using Trizol reagent (Life Technologies); cDNA was generated by reverse transcription (RT) (Quanta Biosciences) from both knockout and wild–type samples. cDNA from each sample was analyzed using quantitative PCR (qPCR) [3]. qPCR experiments were performed using Sybr–Green and sense and antisense primers (Integrated DNA Technologies); primers specific to Cav1, Nav1, and NALCN channels were designed to generate PCR products between 120–200 base pairs. qPCR cycling parameters were: 1 cycle at 95°C for 3 minutes, followed by 40 cycles each consisting of 15 seconds at 94°C, 1 minute at 60°C, 30 seconds at 72°C, followed Sybr Green fluorescence reading. After the completion of 40 cycles, each sample was subjected to a melting temperature ($T_m$) curve analysis. Expression level was estimated using the comparative $C_t$ approximation method to calculate relative abundance of mRNA. Samples were run in triplicate for accuracy and normalized to expression levels of seven housekeeping genes in order to obtain the delta $C_t$. Relative ion channel mRNA abundance was calculated by the equation $2^{-\Delta Ct}$ .

### Immunostaining

Wild–type were perfused transcardially with 4% paraformaldehyde in 0.1 M phosphate buffer, pH 7.3. Brains were removed, thin brain sections (50 μm–thick) were obtained using a Leica vibratome VT1200S. Sections were blocked in 5% normal goat serum followed by incubation with a monoclonal antibody against tyrosine hydroxylase (TH) (16–18 hrs at 4°C, working dilution of 1:1000, Immunostar) and a polyclonal antibody against dopamine–β–hydroxylase (DBH) (16–18 hrs at 4°C working dilution 1:1000, Immunostar). Staining was visualized with the respective secondary antibody conjugated to Alexa 594 or 405 (2 hrs incubation at room temperature, working dilution 1:1000) (Life Technologies). For biocytin experiments, LC neurons were filled with biocytin and stained with Streptavidin conjugated with Alexa 594. Images were acquired with a Fluoview confocal microscope (Olympus) and stored at 12–bit image depth at a resolution of 1024×1024 pixels.

### Pharmacological reagents and channel ligands

Reagents were purchased from Sigma except for isradipine, L–NNA, DTT, ryanodine, orexin, muscimol, and CGP37157 were purchased from R&D Systems; TMRM, Alexa568, Alexa594, and Fluo4 obtained from Life Technologies; genipin was obtained from Wako Reagents, and Ru360 obtained from EMD Biosciences. L–NAME was purchased from Sigma–Aldrich. Drugs stock solutions were prepared in deionized water, DMSO, ethanol, or methanol as instructed by manufacturer on the day of experiment. Stocks were diluted to final concentrations in ACSF to achieve a final solvent concentration of <0.01% v/v.

### Statistical analysis

Imaging data collected was analyzed with Igor Pro 6.0 (Wavemetrics), Matlab (Mathworks), or GraphPad Prism Version 5.0 (GraphPad Software). The stimulation, display, and analysis

software for the two–photon imaging data was analyzed using a custom–written shareware package, WinFluor, PicViewer and PowerCAL kindly provided by John Dempster (Strathclyde University, Glasgow, Scotland; UK). Data were summarized using box–plots showing median values for small sample sizes and the interquatile range to describe the distribution of the data. Sample "n" represents the number of neurons collected from brain slices from at least three mice, one brain slice per mouse. Sample size was determined based on initial effect size, and as reported in previous publications[11]. No randomization of samples was employed. Statistical analysis was performed with GraphPad Prism Version 5.0 (GraphPad Software) using non–parametric tests. Probability (p) threshold for statistical significance was p<0.05.

## Supplementary Material

Refer to Web version on PubMed Central for supplementary material.

## Acknowledgments

## References

1. Aston–Jones G, Cohen JD. An integrative theory of locus coeruleus–norepinephrine function: adaptive gain and optimal performance. Annu Rev Neurosci. 2005; 28:403–450. [PubMed: 16022602]

2. Sara SJ. The locus coeruleus and noradrenergic modulation of cognition. Nat Rev Neurosci. 2009; 10:211–223. [PubMed: 19190638]

3. Park A, Stacy M. Non–motor symptoms in Parkinson's disease. J Neurol. 2009; 256(Suppl 3):293–298.

4. Surmeier DJ, Guzman JN, Sanchez–Padilla J. Calcium, cellular aging, and selective neuronal vulnerability in Parkinson's disease. Cell Calcium. 2010; 47:175–182. [PubMed: 20053445]

5. Nicholls DG. Oxidative stress and energy crises in neuronal dysfunction. Ann N Y Acad Sci. 2008; 1147:53–60. [PubMed: 19076430]

6. Bender A, et al. High levels of mitochondrial DNA deletions in substantia nigra neurons in aging and Parkinson disease. Nat Genet. 2006; 38:515–517. [PubMed: 16604074]

7. Abou–Sleiman PM, Muqit MMK, Wood NW. Expanding insights of mitochondrial dysfunction in Parkinson's disease. Nat Rev Neurosci. 2006; 7:207–219. [PubMed: 16495942]

8. Kubota C, et al. Constitutive Reactive Oxygen Species Generation from Autophagosome/Lysosome in Neuronal Oxidative Toxicity. Journal of Biological Chemistry. 2009; 285:667–674. [PubMed: 19850931]

9. Surmeier DJ, Guzman JN, Sanchez–Padilla J, Goldberg JA. The origins of oxidant stress in Parkinson's disease and therapeutic strategies. Antioxid Redox Signal. 2011; 14:1289–1301. [PubMed: 20712409]

10. Surmeier DJ, Guzman JN, Sanchez J, Schumacker PT. Physiological phenotype and vulnerability in Parkinson's disease. Cold Spring Harb Perspect Med. 2012; 2:a009290. [PubMed: 22762023]

11. Guzman JN, et al. Oxidant stress evoked by pacemaking in dopaminergic neurons is attenuated by DJ–1. Nature. 2010; 468:696–700. [PubMed: 21068725]

12. Verkhratsky A. The endoplasmic reticulum and neuronal calcium signalling. Cell Calcium. 2002; 32:393–404. [PubMed: 12543098]

13. McCormack JG, Halestrap AP, Denton RM. Role of calcium ions in regulation of mammalian intramitochondrial metabolism. Physiol Rev. 1990; 70:391–425. [PubMed: 2157230]

14. Williams JT, North RA, Shefner SA, Nishi S, Egan TM. Membrane properties of rat locus coeruleus neurones. Neuroscience. 1984; 13:137–156. [PubMed: 6493483]

15. Filosa JA, Putnam RW. Multiple targets of chemosensitive signaling in locus coeruleus neurons: role of K+ and Ca2+ channels. Am J Physiol Cell Physiol. 2003; 284:C145–55. [PubMed: 12388081]

16. Imber AN, Putnam RW. Postnatal development and activation of L–type Ca2+ currents in locus ceruleus neurons: implications for a role for Ca2+ in central chemosensitivity. J Appl Physiol. 2012; 112:1715–1726. [PubMed: 22403350]

17. Christie MJ, Williams JT, North RA. Electrical coupling synchronizes subthreshold activity in locus coeruleus neurons in vitro from neonatal rats. J Neurosci. 1989; 9:3584–3589. [PubMed: 2795142]

18. North RA, Williams JT. Opiate activation of potassium conductance inhibits calcium action potentials in rat locus coeruleus neurones. Br J Pharmacol. 1983; 80:225–228. [PubMed: 6652378]

19. Kang S, et al. Structure–activity relationship of N,N'–disubstituted pyrimidinetriones as Ca(V)1.3 calcium channel–selective antagonists for Parkinson's disease. J Med Chem. 2013; 56:4786–4797. [PubMed: 23651412]

20. Guzman JN, Sanchez–Padilla J, Chan CS, Surmeier DJ. Robust pacemaking in substantia nigra dopaminergic neurons. J Neurosci. 2009; 29:11011–11019. [PubMed: 19726659]

21. Foehring RC, Zhang XF, Lee JCF, Callaway JC. Endogenous calcium buffering capacity of substantia nigral dopamine neurons. J Neurophysiol. 2009; 102:2326–2333. [PubMed: 19675297]

22. Maravall M, Mainen ZF, Sabatini BL, Svoboda K. Estimating intracellular calcium concentrations and buffering without wavelength ratioing. Biophys J. 2000; 78:2655–2667. [PubMed: 10777761]

23. Fierro L, Llano I. High endogenous calcium buffering in Purkinje cells from rat cerebellar slices. J Physiol (Lond). 1996; 496(Pt 3):617–625. [PubMed: 8930830]

24. Dooley CT, et al. Imaging Dynamic Redox Changes in Mammalian Cells with Green Fluorescent Protein Indicators. Journal of Biological Chemistry. 2004; 279:22284–22293. [PubMed: 14985369]

25. Wang H–Q, Takahashi R. Expanding insights on the involvement of endoplasmic reticulum stress in Parkinson's disease. Antioxid Redox Signal. 2007; 9:553–561. [PubMed: 17465880]

26. Patergnani S, et al. Calcium signaling around Mitochondria Associated Membranes (MAMs). Cell Commun Signal. 2011; 9:19. [PubMed: 21939514]

27. Brand MD, et al. Mitochondrial superoxide and aging: uncoupling–protein activity and superoxide production. Biochem Soc Symp. 2004:203–213. [PubMed: 15777023]

28. Cookson MR. Parkinsonism due to mutations in PINK1, parkin, and DJ–1 and oxidative stress and mitochondrial pathways. Cold Spring Harb Perspect Med. 2012; 2:a009415. [PubMed: 22951446]

29. Goldberg JA, et al. Calcium entry induces mitochondrial oxidant stress in vagal neurons at risk in Parkinson's disease. Nature Neuroscience. 2012; 15:1414–1421. [PubMed: 22941107]

30. Samuels ER, Szabadi E. Functional neuroanatomy of the noradrenergic locus coeruleus: its roles in the regulation of arousal and autonomic function part II: physiological and pharmacological manipulations and pathological alterations of locus coeruleus activity in humans. Curr Neuropharmacol. 2008; 6:254–285. [PubMed: 19506724]

31. Berridge CW, España RA, Vittoz NM. Hypocretin/orexin in arousal and stress. Brain Res. 2010; 1314:91–102. [PubMed: 19748490]

32. Horvath TL, et al. Hypocretin (orexin) activation and synaptic innervation of the locus coeruleus noradrenergic system. J Comp Neurol. 1999; 415:145–159. [PubMed: 10545156]

33. van den Pol AN, et al. Hypocretin (orexin) enhances neuron activity and cell synchrony in developing mouse GFP–expressing locus coeruleus. J Physiol (Lond). 2002; 541:169–185. [PubMed: 12015428]

34. Soffin EM, et al. SB–334867–A antagonizes orexin mediated excitation in the locus coeruleus. Neuropharmacology. 2002; 42:127–133. [PubMed: 11750922]

35. Murphy MP. How mitochondria produce reactive oxygen species. Biochem J. 2009; 417:1–13. [PubMed: 19061483]

36. Marks JD, Boriboun C, Wang J. Mitochondrial nitric oxide mediates decreased vulnerability of hippocampal neurons from immature animals to NMDA. J Neurosci. 2005; 25:6561–6575. [PubMed: 16014717]

37. Traaseth N, Elfering S, Solien J, Haynes V, Giulivi C. Role of calcium signaling in the activation of mitochondrial nitric oxide synthase and citric acid cycle. Biochim Biophys Acta. 2004; 1658:64–71. [PubMed: 15282176]

38. White RJ, Reynolds IJ. Mitochondria accumulate Ca2+ following intense glutamate stimulation of cultured rat forebrain neurones.

39. Waypa GB, et al. Hypoxia Triggers Subcellular Compartmental Redox Signaling in Vascular Smooth Muscle Cells. Circulation Research. 2010; 106:526–535. [PubMed: 20019331]

40. Nedergaard S, Flatman JA, Engberg I. Nifedipine– and omega–conotoxin–sensitive Ca2+ conductances in guinea–pig substantia nigra pars compacta neurones. J Physiol (Lond). 1993; 466:727–747. [PubMed: 8410714]

41. Wilson CJ, Callaway JC. Coupled oscillator model of the dopaminergic neuron of the substantia nigra. J Neurophysiol. 2000; 83:3084–3100. [PubMed: 10805703]

42. Berridge MJ. The endoplasmic reticulum: a multifunctional signaling organelle. Cell Calcium. 2002; 32:235–249. [PubMed: 12543086]

43. Mosharov EV, et al. Interplay between cytosolic dopamine, calcium, and alpha–synuclein causes selective death of substantia nigra neurons. Neuron. 2009; 62:218–229. [PubMed: 19409267]

44. Samuels ER, Szabadi E. Functional neuroanatomy of the noradrenergic locus coeruleus: its roles in the regulation of arousal and autonomic function part I: principles of functional organisation. Curr Neuropharmacol. 2008; 6:235–253. [PubMed: 19506723]

45. Aston–Jones G, Bloom FE. Activity of norepinephrine–containing locus coeruleus neurons in behaving rats anticipates fluctuations in the sleep–waking cycle. J Neurosci. 1981; 1:876–886. [PubMed: 7346592]

46. Gargaglioni LH, Hartzler LK, Putnam RW. The locus coeruleus and central chemosensitivity. Respir Physiol Neurobiol. 2010; 173:264–273. [PubMed: 20435170]

47. Surmeier DJ, Guzman JN, Sanchez–Padilla J, Goldberg JA. The origins of oxidant stress in Parkinson's disease and therapeutic strategies. Antioxid Redox Signal. 2011; 14:1289–1301. [PubMed: 20712409]

48. Wardman P. Fluorescent and luminescent probes for measurement of oxidative and nitrosative species in cells and tissues: progress, pitfalls, and prospects. Free Radic Biol Med. 2007; 43:995–1022. [PubMed: 17761297]

49. Becker C, Jick SS, Meier CR. Use of antihypertensives and the risk of Parkinson disease. Neurology. 2008; 70:1438–1444. [PubMed: 18256367]

50. Anekonda TS, Quinn JF. Calcium channel blocking as a therapeutic strategy for Alzheimer's disease: the case for isradipine. Biochim Biophys Acta. 2011; 1812:1584–1590. [PubMed: 21925266]
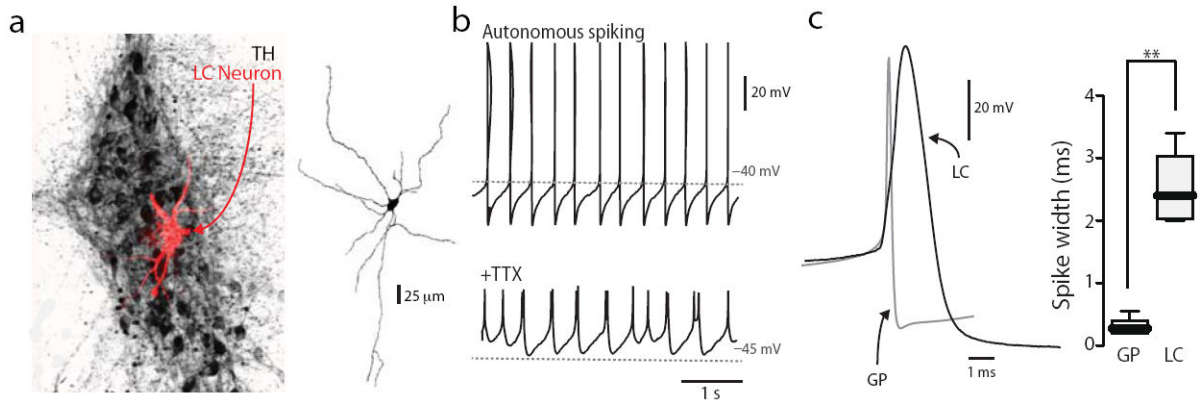
**Figure 1. LC neurons were autonomous pacemakers with broad action potential spikes**
(a) Biocytin–labeled neuron (red, stained with streptavidin–conjugated to alexa594) colocalised with neurons immunoreactive for the LC biomarker tyrosine hydroxylase (TH). To the right, a representative reconstruction of a biocytin–filled LC neuron is shown. (b) Representative LC recording displaying autonomous spiking activity, recordings performed in the presence of glutamate and GABA receptor synaptic blockers. Bottom panel shows a representative trace of LC recording with spikelet activity following blockade of Nav1 channels with TTX (1 μM). Under our recording conditions, more than 90% of the LC neurons recorded displayed spikelet activity (n=20 neurons, from 10 mice). (c) Representative traces showing spike width in LC neurons (n=5 neurons, from 3 mice, median=2.4 sec) compared to globus pallidus (GP) neurons (n=6 neurons, from 3 mice, median=0.28 sec). Right panel shows box–plot quantification with spike widths in LC neurons significantly wider than GP neurons (p=0.004). Data presented as whisker box plots displaying median and interquartile ranges, and analyzed using Mann-Whitney test
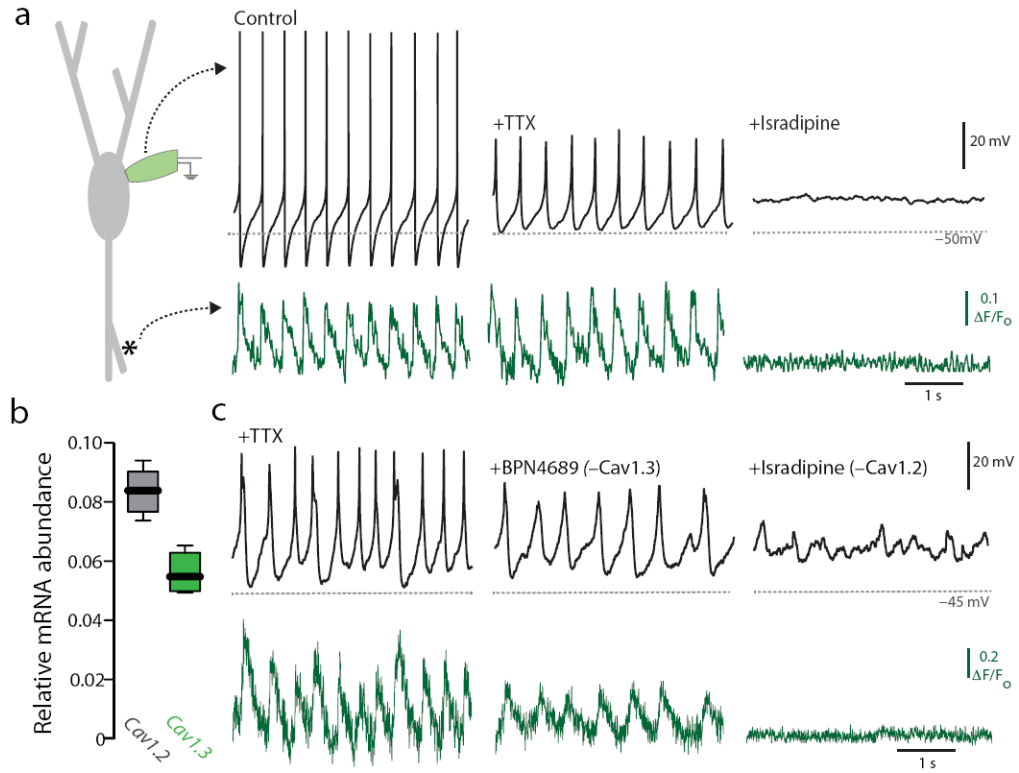
**Figure 2. Engagement of L–type channels mediated dendritic $Ca^{2+}$ oscillations during spiking activity in LC**

(a) Left panel shows a schematic of an LC neuron illustrating of our whole–cell current clamp–recording configuration of spiking activity synchronized to 2PLSM dendritic $Ca^{2+}$ line–scan imaging. Spiking activity is accompanied with phase–locked $Ca^{2+}$ oscillations in distal dendrites (80–100 μm away from soma), detected in full–spike mode (control) or in the presence of TTX. Antagonism of L–type $Ca^{2+}$ channels with 1 μM isradipine eliminates $Ca^{2+}$ oscillations in the presence of TTX (n=4 neurons from 4 mice; p<0.001, Wilcoxon matched–pairs signed rank test). (b) Quantitative PCR analysis demonstrates mRNA expression of both *Cav1.2* and *Cav1.3* L–type channel subunits in LC neurons (n=6 mice). (c) Representative spiking activity traces in the presence of TTX before and after selective antagonism of Cav1.3 channels with 50 μM BPN4689, and non–selective antagonism of Cav1.2 and Cav1.3 with 1 μM isradipine. Antagonism of Cav1.3 channels with BPN4689 significantly decreased spike amplitude (p=0.017), frequency (p=0.018), and amplitude of dendritic $Ca^{2+}$ oscillations (p=0.023) in LC neurons (n=5 neurons from 5 mice). Residual spiking activity and $Ca^{2+}$ oscillations were attenuated completely by 1 μM isradipine suggesting that Cav1.2 channels mediated the residual activity (p<0.001). Data presented as whisker box plots displaying median and interquartile ranges, and analyzed using Mann-Whitney test.
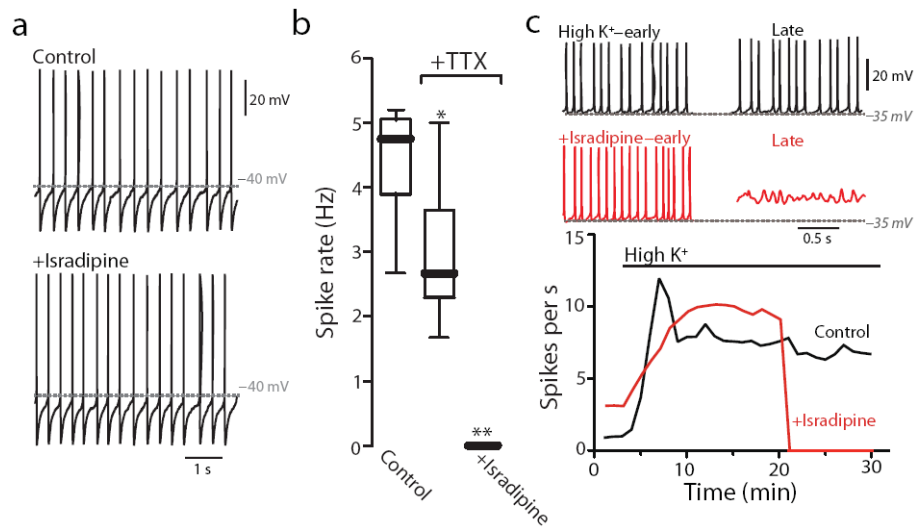
**Figure 3. L–type Ca$^{2+}$ channels were not essential to sustain autonomous spiking but necessary under conditions of elevated spike rate**

(a) Representative traces showing that antagonism of L–type channels with isradipine (5 μM) does not affect spike rate in LC neurons (n=4 neurons from 4 mice, p=0.700). (b) Box–plot quantification showing blockade of Nav1 channels slows down spike rate (p=0.032), and leaving smaller amplitude spikelets attenuated by antagonism of L–type Ca$^{2+}$ channels with isradipine (1 μM) (n=10 neurons from 10 mice, p<0.001). (c) Representative perforated–patch current clamp recordings of LC neurons following high potassium (K$^{+}$), leading to elevated spike rate. Under control conditions (n=3 neurons from 3 mice), elevated spike rate is sustained for as long as recordings were held. In the presence of 500 nM isradipine, LC neurons failed to continue spiking after 20 minutes of high K$^{+}$ (n=3 neurons from 3 mice), suggesting that L–type channels are necessary during periods of elevated spike rates. Data presented as whisker box plots displaying median and interquartile ranges, and analyzed using Mann-Whitney test.
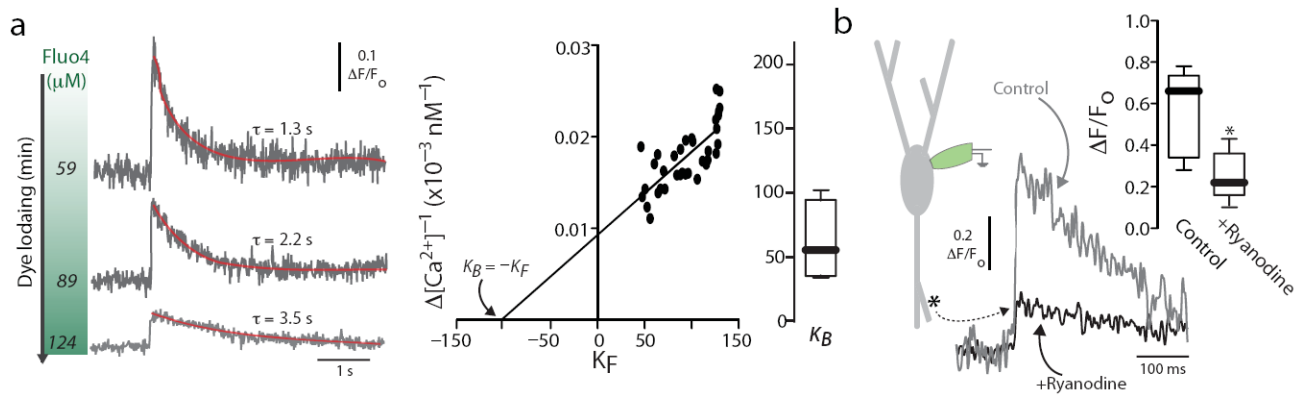
**Figure 4. Endoplasmic reticulum sequestered cytosolic Ca$^{2+}$ under conditions of low intrinsic Ca$^{2+}$ buffering**

(a) Representative somatic Ca$^{2+}$ transients evoked by single spikes sampled at different concentrations of Fluo4. Ca$^{2+}$ transients displayed decreased transient amplitude and increased decay time with increasing Fluo4. The change in intracellular Ca$^{2+}$ concentration ($[\Delta Ca^{2+}]$) was calculated and then plotted against the calculated added extrinsic buffer ($K_F$) (middle panel), and data points were fitted using a linear regression to compute endogenous buffering capacity ($K_B$), calculated from the negative x–intercept. Box plot quantification revealed a median $K_B$ in LC neurons of 58 (n=4 neurons from 4 mice). (b)Representative dendritic Ca$^{2+}$ traces averaged from pacemaking spike–triggered Ca$^{2+}$ transients before and after antagonism of ryanodine receptors (RyR) with 10 μM ryanodine. Antagonism of RyRs significantly decreased the amplitude of Ca$^{2+}$ transients, consistent with Ca$^{2+}$–induced Ca$^{2+}$ release (CICR) occurring during autonomous spiking (n=5 neurons from 5 mice, p=0.028). Data presented as whisker box plots displaying median and interquartile ranges, and analyzed using Mann-Whitney test.
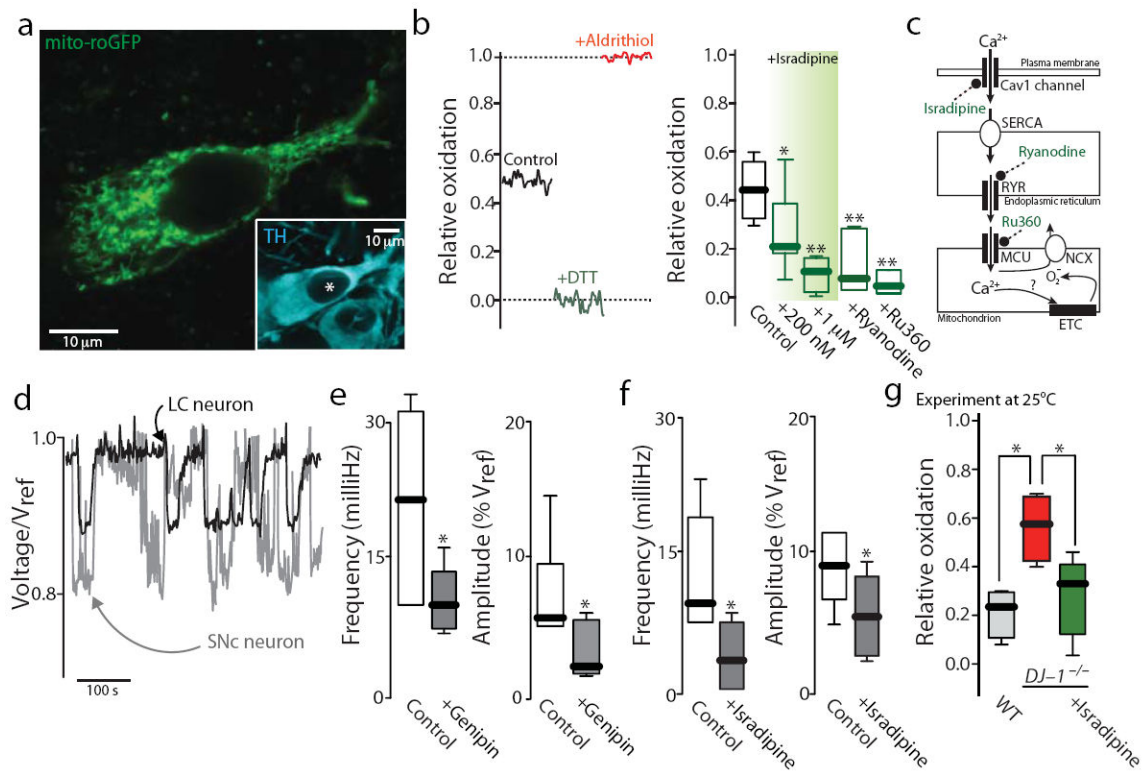
**Figure 5. L–type channels triggered mitochondrial oxidant stress in LC**

(a) Mito–roGFP positive LC neuron immunoreactive to tyrosine hydroxylase (TH). (b) Mito-roGFP calibration with relative oxidation of 0.4. Isradipine attenuated oxidation in a dose-dependent manner (n=5 neurons control, 5 mice, n=4 neurons 200 nM isradipine, 4 mice, p=0.028; n=5 neurons 1 μM isradipine, 4 mice, p=0.002). Ryanodine (n=6 neurons, 5 mice, p=0.001) and Ru360 (n=4 neurons,4 mice, p=0.007) also attenuated mitochondrial oxidation. (c) $Ca^{2+}$ entry through L–channels is pumped into ER via the sarcoendoplasmic reticulum $Ca^{2+}$ ATPase (SERCA). Mitochondrial–associated–membranes (MAMs) allow $Ca^{2+}$release from inositol–1,4,5–trisphosphate receptors (IP$_3$Rs) and RyRs into the mitochondria through MCU. (d)Mitochondrial–membrane potential (MMP) oscillations of LC and SNc neurons using TMRM. (e) UCPs antagonized with genipin (100 μM) attenuated the amplitude (p=0.031) and frequency (p=0.016) of MMP oscillations. (f) Isradipine decreased the amplitude (p=0.047) and frequency (p=0.017) of MMP oscillations. Panel e–f , n=6 neurons, 3 mice per antagonist, Wilcoxon–matched pairs signed rank test. (g) Loss of *DJ–1* function (*DJ–1$^{-/-}$*) exacerbated mitochondrial oxidant stress in *DJ–1$^{-/-}$* (red) compared to WT (p=0.029, n=4 WT neurons, 3 mice, n=4 *DJ–1$^{-/-}$* neurons, 3 mice). Neurons with 1 μM isradipine (green) for 1 hr attenuated oxidant stress in *DJ–1$^{-/-}$* (p=0.032, n=5 *DJ–1$^{-/-}$* neurons with isradipine, 3 mice), Data presented as whisker box plots with median and interquartile ranges, and analyzed using Mann-Whitney test compared to control.
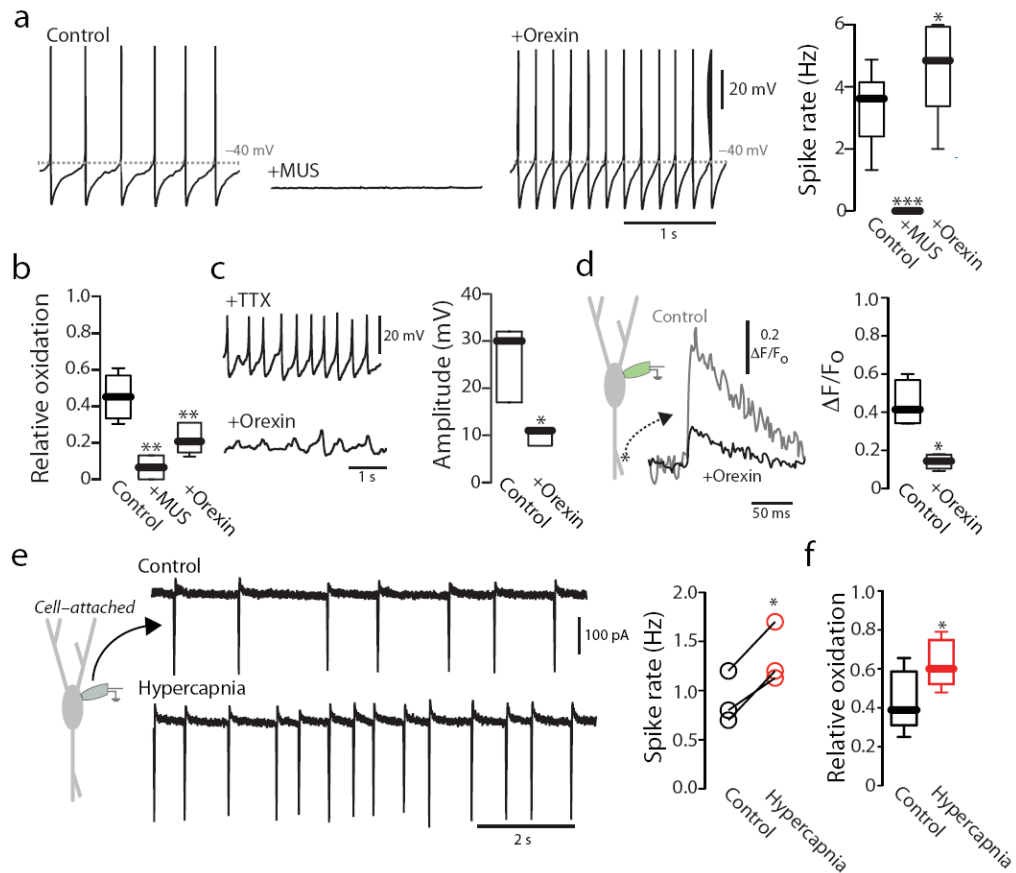
**Figure 6. Modulation of spiking and mitochondrial oxidant stress**

(a) Muscimol (10 μM, MUS) silenced pacemaking whereas orexin (500 nM) nearly doubled spike rate compared to control (n=4 neurons from 2 mice with MUS, p=0.002; n=8 neurons orexin from 8 mice, p=0.022,). (b) Muscimol and orexin decreased relative oxidation in LC neurons (n=5 control neurons from 5 mice; n=4 neurons with MUS from 3 mice, p=0.003; n=6 orexin-treated neurons from 3 mice, p=0.010). (c) Orexin attenuated spikelet amplitude in LC neurons (n=4 neurons from 4 mice, p=0.038). (d) Dendritic $Ca^{2+}$ traces averaged from pacemaking–triggered $Ca^{2+}$ transients before and after bath application of orexin. Orexin decreased the amplitude of dendritic $Ca^{2+}$ transients despite an increase in spike rate (n=4 neurons from 4 mice, p=0.014). (e) Pacemaking firing in LC neurons recorded in cell–attached mode under control conditions of 95% oxygen and 5% carbon dioxide, pH 7.4, or hypercapnia, induced by bubbling ACSF with a gas mixture of 85% oxygen and 15% carbon dioxide. From the 3 neurons (from 3 mice) recorded before and after hypercapnia, all three neurons increased spike rate under hypercapnic conditions (p=0.038). (f) LC neurons exposed to 1 hour of hypercapnia (n=8 neurons from 3 mice, p=0.023) displayed increased mitochondrial oxidant stress when compared to control neurons (n=5 neurons from 3 mice). Data presented as whisker box plots displaying median and interquartile ranges, and analyzed using Mann-Whitney test comparing to respective controls.
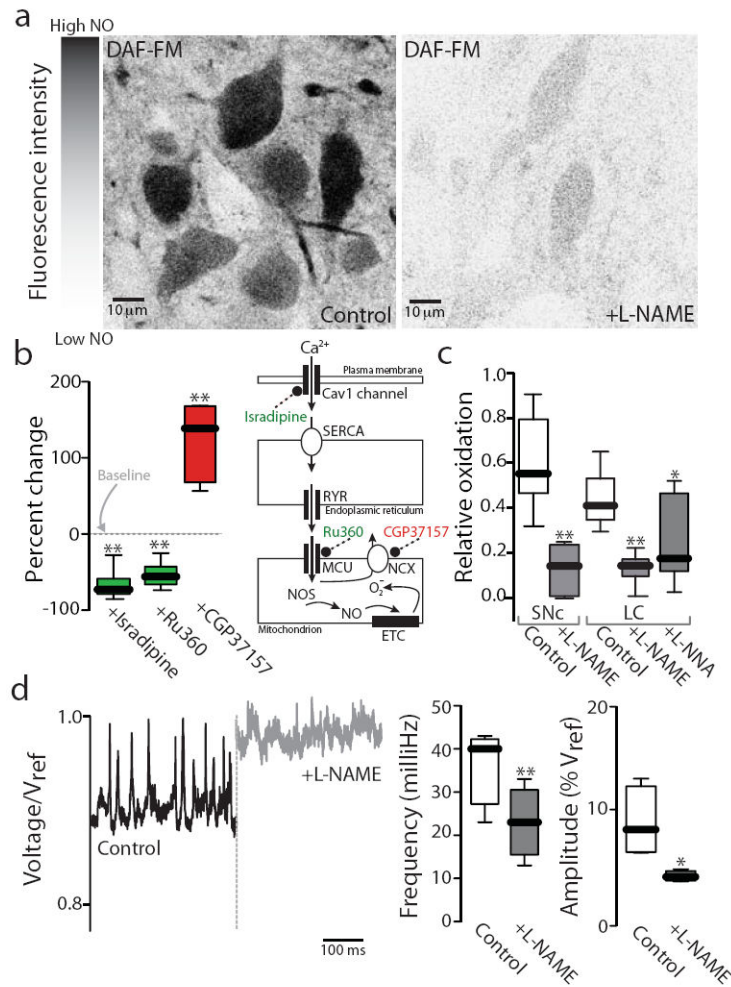
**Figure 7. Nitric oxide synthase contributed to oxidant stress**

(a) LC neurons labeled with the nitric oxide (NO) fluorescent probe DAF–FM with 100 μM L–NAME relative to control (n=3 mice). L–NAME attenuated NO production shown as decreased DAF-FM fluorescence. (b) NO production was decreased with isradipine (1 μM) or Ru360 (10 μM) (n=7 neurons isradipine, p=0.002; n=8 neurons Ru360, p=0.002, data collected from 3 mice). Antagonism of mitochondrial $Na^+$–$Ca^{2+}$ exchange (NCX) with 5 μM CGP37157 led to enhanced production of NO (n=6 neurons from 3 mice with CGP37157, p=0.001). Schematic displays the signals tracing Cav1 channel-mediated $Ca^{2+}$ entry to increased intramitochondrial $Ca^{2+}$. $Ca^{2+}$-induced stimulation of NO impairs ETC and leads to generation of mitochondrial oxidant stress. (c) NOS inhibition in SNc and LC neurons decrease mitochondrial oxidant stress (n=7 control SNc neurons from 5 mice, n=6 L–NAME–treated SNc neurons from 5 mice, p<0.001; n=6 L–NAME–treated LC neurons from 4 mice, p=0.007). Control relative oxidation values of LC neurons were replotted from fig. 5b for comparison purposes. A different NOS inhibitor, L–NNA (10 μM) also decreased mitochondrial oxidation in LC (n=6 L–NNA treated neurons from 4 mice, p=0.036). (d) L–NAME decreased the amplitude (p=0.029)and frequency (p=0.014)of mitochondrial membrane potential oscillations in LC neurons measured with TMRM (n=4 neurons from 4

mice). Data presented as whisker box plots displaying median and interquartile ranges, and analyzed using Mann-Whitney test relative to controls.